ACS APPLIED MATERIALS & INTERFACES

Research Article

www.acsami.org

Charge Transport Properties in TiO_2 Network with Different Particle Sizes for Dye Sensitized Solar Cells

Kwangsuk Park, Qifeng Zhang, Daniel Myers, and Guozhong Cao*

Department of Materials Science and Engineering, University of Washington, Seattle, Washington 98195, United States

Supporting Information

ABSTRACT: The charge transport properties in the TiO_2 nanoparticle networks with the different TiO_2 nanoparticle sizes were investigated by means of electrochemical impedance spectroscopy (EIS) with consideration of morphological aspects of mesoporous TiO_2 network including particle size (d_p), coordination number (N_n), neck diameter (d_n), and effective surface area (S_e). The morphological analysis of the network revealed that the particle size and surface area would be factors exerting an impact on the charge transport properties, while the coordination number and neck diameter seemed to be consistent with the nanoparticle size. As a result, the electron transport along with the TiO_2 network was predominantly affected by the particle size in terms of the mean free path; the bigger particle size provides both long travel distance and less collision chance with the boundary. Surface area seems to exert a strong influence on the recombination when it is in contact with an electrolyte, suggesting that pore size distribution determining penetration of an electrolyte has to be considered in terms of the effective surface area (S_e). Due to the low transport resistance, high recombination resistance, and low chemical capacitance, the largest particle showed the longest diffusion length (L_n). However, the highest efficiency observed in 15 nm TiO_2 nanoparticle photoanode indicated that the compensating characteristics of the morphological factors of the network for light harvesting efficiency (LHE) (surface area) and charge collection efficiency (η_c, particle size) should be balanced in designing a nanostructured network for high performance DSCs.

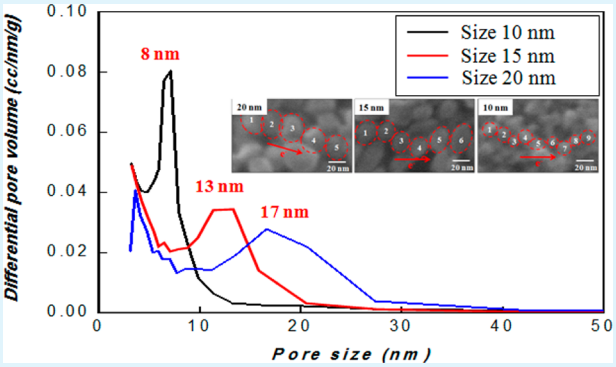

KEYWORDS: *dye sensitized solar cells, nanoparticle size, impedance, charge transport properties*

INTRODUCTION

Since the large improvement in performance of dye sensitized solar cells (DSCs) achieved in 1991, mesoporous networks composed of nanostructured oxides have intensively been studied using developments in nanotechnologies.[1−5] Due to the huge specific surface area of a mesoporous network, even the case where monolayered dye molecules are adsorbed on the surface of a network, such a high photocurrent as much as 20 mA/cm^2 was achieved as a result of high dye loading as well as reduced electron injection distance, in which each of them is responsible for good light harvesting and electron injection, respectively.[6] Also, spatial separation of electron−hole pairs in DSCs enables the electrons injected into conduction band of an oxide network to be collected on a semiconducting substrate effectively in spite of the high grain boundary and surface area of an oxide network which have been considered to impede charge transport and accelerate electron back flow (recombination). Thus, further improvement of DSCs has been tried by varying morphologies of nanomaterials from nanoparticle to nanorod and nanotube because these morphologies can provide better charge separation and transport. Even though the one-dimensional nanostructures were proven to have better charge transport properties, the nanoparticle structure still shows the best performance of DSCs.[7,8]

Once electrons are injected into the conduction band of an oxide from excited dye molecules, they experience two types of processes: transport and recombination. Transport is a forward movement of electrons to a collector as a result of gradient of electron concentration, whereas recombination is a back flow of electrons to oxidized dyes and tri-iodide ions. Competition between transport and recombination can be denoted as charge collection efficiency (η_c), indicating how many electrons can be collected at a conducting metal oxide substrate before recombination. Transport of electrons in an oxide network occurs mainly through diffusion with numerous trapping−detrapping events, whose characteristics are commonly explained by a multiple trapping (MT) model. In the MT model, electrons are considered to be mostly trapped (>90% of injected electrons) at localized states and escape from them by thermal activation. This suggests that the trap sites affecting electron transport would be mainly shallow traps located either at grain boundaries or at defects in the oxide network, while deep traps located 0.5 eV below the conduction band would

Received: November 20, 2012
Accepted: January 22, 2013
Published: January 22, 2013

not contribute to electron transport due to the required high thermal activation energy.[9−11]

A mesoporous oxide film is usually formed by depositing a paste containing oxide nanoparticles on a fluorine-doped tin oxide (FTO) substrate, followed by sintering at a moderate temperature. The morphologies or porous structure of the resulting oxide film are mainly determined by the nanoparticles and annealing conditions. Figure 1 schematically illustrates a

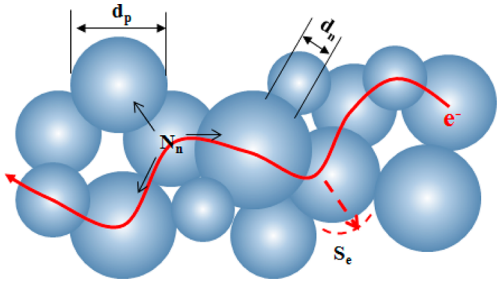

Figure 1. Schematic illustrating electron transport occurring in a network; *n* particle and through neck, including structural parameters of an oxide network affecting electron transport such as particle size (d_p), neck diameter (d_n), and coordination number (N_n). Recombination occurs through the surface of an oxide network in contact with an electrolyte (S_e).

nanoparticle network including factors affecting charge transport. In a network composed of numerous nanoparticles, electrons have to experience transport in one particle and transfer to an adjacent particle through the neck formed between them to be collected at a semiconducting substrate. However, the characteristics of the high surface area and boundary of an oxide network give rise to unfavorable charge transport phenomena: electron reflection and recombination at a boundary and/or surface. From this perspective, four main parameters of an oxide network affecting charge transport can be inferred as follows: (1) particle size (d_p), which determines diffusion distance of electrons before meeting boundary where they are reflected, (2) effective surface area (S_e), where recombination and/or reflection of electrons occur, (3) neck diameter (d_n) as a pathway for electron transfer from one particle to the other, and (4) coordination number (N_n) denoting the number of the pathway. Aside from the effect of the morphological aspects on charge transport, the trapping−detrapping process is also affected.

Electron transport from one particle to another could occur through a two step process; electrons travel inside one particle to reach the surface of a particle and, then, transfer from one particle to the adjacent particle through a neck formed between them, suggesting that a larger particle and neck size are desirable for good electron transport as electrons can travel longer in particles and escape easier from one particle through paths with larger widths. A 32 nm particle film displayed almost 4 times higher diffusion coefficient than a 14 nm one due to the reduced boundaries such as surface area and grain boundary.[12] Also, a larger TiO_2 nanoparticle film showed good resistance to recombination as a result of longer diffusion length of electrons in TiO_2 nanoparticle film.[13] Monte Carlo random walk model revealed that more time is needed to extract an electron from a narrow neck than a wide one as well as partial ordering introduced into a random network improves charge collection efficiency, indicating that controlling electron transport from one particle to an adjacent particle would be a good strategy for better performance of DSCs.[14,15] Recently, the same simulation method argued charge transport in the mesoporous network is more dependent on electronic structure than geometric effect.[16] However, it is known that the electronic structure of a mesoporous film is also affected by the morphological aspects of a film.[17,18] Coordination number (N_n) also exerts a positive impact on electron transport in terms of the number of ways electrons can pass through a given particle. Higher charge mobility in anatase than in rutile is ascribed to more coordination numbers (N_n).[19] Also, constricted effect of necks between particles on charge transport was discussed through simulating network structures with different coordination number.[20] However, as each structural parameter does not work independently, contributions of these structural parameters to the performances of DSCs are not straightforward. For example, larger particle size, which facilitates charge transport, would be detrimental to the power conversion efficiency of DSC due to reduced surface area and the resulting reduction in light harvesting efficiency (LHE).

The previous works demonstrated that the particle size and resultant pore size, neck, and/or boundary (surface area) exerts a considerable impact on performance of DSCs in terms of electron injection, transport, recombination, and dye adsorption.[12,13,21,22] However, most works were carried out without careful consideration on morphological parameters of a network such as porosity (coordination number, N_n) and neck between TiO_2 nanoparticles and surface area (S). To achieve reliable information on the morphology of the networks composed of different sized TiO_2 nanoparticles, in this study, preparation of the samples for BET measurement was specially designed, and then, the obtained morphological information of the TiO_2 networks composed of different TiO_2 nanoparticle sizes was utilized as critical factors affecting charge transport properties as well as electronic structure of the TiO_2 nanoparticle networks through electrochemical impedance spectroscopy (EIS).

EXPERIMENTAL PROCEDURES

Synthesis of TiO_2 Nanoparticles. The nanoparticle samples were prepared through a hydrothermal treatment of a TiO_2 aqueous sol containing 0.05 M titanium isopropoxide, 0.1 M HCl, and 0.01 M surfactant (IGEPAL CO-520). The sizes of nanoparticles were controlled by changing the temperature and time of hydrothermal treatment. The conditions for the nanoparticles of different size were as follows: 180 °C (2 h) for 10 nm, 200 °C (5 h) for 15 nm, and 240 °C (24 h) for 20 nm. The precipitate was washed with water and ethanol several times and then dried at 100 °C for 10 h to achieve the final product in powder form.

Fabrication of Solar Cells. A doctor blade method was used to make a TiO_2 film on a FTO glass. TiO_2 nanoparticle pastes were prepared by mixing ground TiO_2 nanoparticles in acetic acid, deionized water, ethanol, and α-terpineol with 10 wt % ethyl cellulose in ethanol. Doctor bladed paste layer on FTO glass was first dried at 150 °C for 10 min and then annealed at 450 °C for 1 h. The resulting TiO_2 film was sensitized with N719 (Solaronix) by immersing it in an ethanol solution containing 0.3 mM of N719 for 24 h. The sensitized film as a photoanode was assembled with a counter electrode for which a platinum-coated silicon was used. The gap between the two electrodes was filled with a commercial electrolyte containing organic iodide salt, pyridine derivative, and inorganic iodide salt in acetonitrile/valeronitrile solvent (EL-HPE, Dyesol).

Preparation of BET Sample. The TiO_2 nanoparticle paste was prepared as described above and inserted into a preformed glass tube (4 mm diameter, 1 mm wall), followed by annealing at 450 °C for 1 h. (See Figure S1 in the Supporting Information.) The weight of the

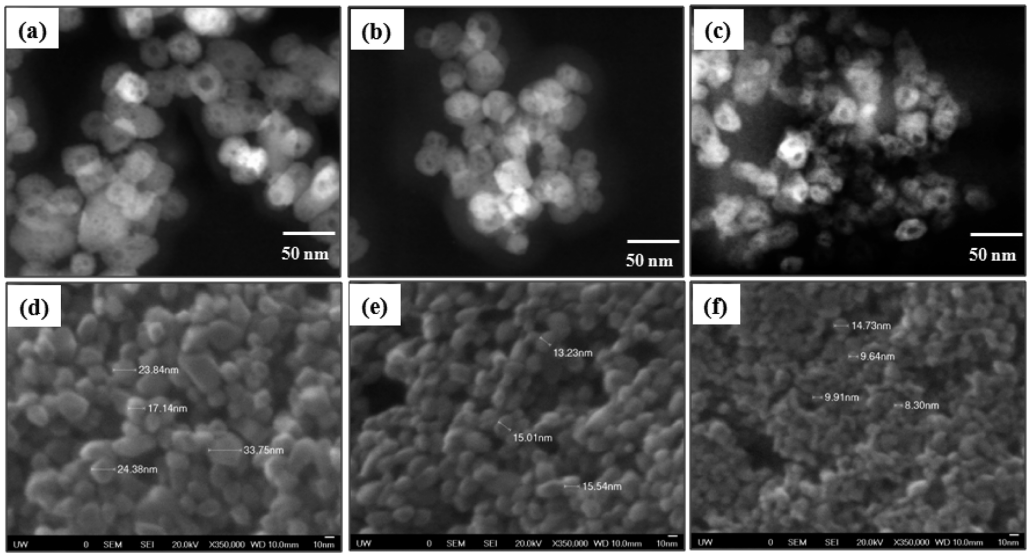

Figure 2. High angle annular dark field (HAADF) TEM images showing TiO_2 nanoparticles of (a) 20 nm, (b) 15 nm, and (c) 10 nm and SEM images displaying morphologies of films composed of (d) 20 nm, (e) 15 nm, and (f) 10 nm TiO_2 nanoparticles.

TiO_2 network in the glass tube was obtained by subtracting the premeasured weight of a glass tube from the total weight of a glass tube containing a TiO_2 network. By inserting the glass tube into a 6 mm BET cell tube, the TiO_2 nanoparticle network can be preserved during BET measurement.

Structural Characterization, Property, and Performance Measurements. TiO_2 nanoparticles were examined through scanning electron microscopy (SEM) and transmission electron microscopy (TEM). The crystallinity of different sized TiO_2 nanoparticles were characterized by X-ray diffraction (XRD). Brunauer–Emmett–Teller (BET, Quantachrome NOVA 4200e) was used to measure physical characteristics of TiO_2 nanoparticle networks including surface area, pore size distribution, and porosity. Dye loading amount was determined by a UV–vis absorption spectrum, where 0.1 M NaOH solution was used to dissolve the dye molecules from the sensitized electrodes. Electrochemical impedance spectroscopy (EIS) was performed using the Solartron 1287A equipped with the Solartron 1260 FRA/impedance analyzer to calculate charge transport properties including electron lifetime, chemical diffusion coefficient, and diffusion length based on chemical capacitance, charge transfer resistance, and diffusion resistance. The measurements were done under a dark condition by varying bias voltage from −0.75 V to −0.6 V, keeping the AC amplitude 10 mV. The frequencies applied ranged from 0.05 to 10^5 Hz. Cyclic voltammetry (CV) was used to characterize the electronic structure of the TiO_2 networks. The CV tests were carried out by immersing TiO_2 films into a pH 2 aqueous electrolyte adjusted with H_2SO_4 under a scan rate of 50 mVs^{-1}. The solar cell performances were characterized by using an HP 4155A programmable semiconductor parameter analyzer under AM 1.5 simulated sunlight with the power density of 100 mW cm^{-2}.

RESULTS AND DISCUSSIONS

Characteristics of TiO_2 Networks. Figure 2 is TEM and SEM images showing the different sized TiO_2 nanoparticles and morphologies of their networks after annealing at 450 °C. The TiO_2 nanoparticle size was increased from about 10 nm to a range of 15–20 nm with increasing process temperature and time, as shown in Figure 2a–c. Each TiO_2 particle kept shape, indicating that the annealing at 450 °C for 1 h only caused the sintering forming neck between particles, not densification resulting in neck growth, which was also supported by SEM images shown in Figure 2d–f where the boundary of each TiO_2 particle was obviously observed. The contrastable difference on the TiO_2 nanoparticles in TEM images simply reflect the thickness difference; the black spot is the area with thinner thickness than others. The TEM samples were prepared by scraping off the TiO_2 particle films formed after annealing at 450 °C and redispersing the TiO_2 nanoparticles in ethanol through sonication; the necks connecting adjacent nanoparticles would be broken and expose the thinner area, which resulted from the grain boundary diffusion induced sintering. The resulting networks' morphologies like porosity and pore size distribution seemed to be affected by the nanoparticle size. Figure 2d–f shows that pores became larger with the increase of the nanoparticle size, which might again change the porosity of the films.

Prior study has shown that the crystallinity of as-grown TiO_2 nanoparticles varies with process conditions; specifically, crystallinity was improved with process temperature.[22] However, as shown in Figure 3, the postannealing at 450 °C for 1 h to form a network structure seems to result in uniform crystallinity of the different sized TiO_2 nanoparticles. The final phase of the TiO_2 nanoparticles was revealed to be uniformly anatase. According to the Scherer formula based on the (101) peak, the calculated particle sizes were revealed to be 18, 14,

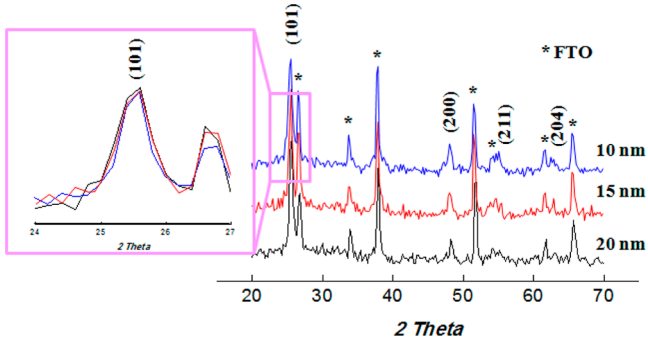

Figure 3. XRD patterns of different sized TiO_2 nanoparticles, indicating all samples are anatase phase. Inset is the enlarged (101) used to calculate the size of theTiO_2 nanoparticles.

and 11 nm, showing the good agreement with the results in Figure 2.

The TiO_2 nanoparticle networks' morphologies were investigated by nitrogen sorption isotherms in terms of surface area, pore size distribution, and porosity. Instead of powdered TiO_2 nanoparticles, the use of the TiO_2 nanoparticle networks formed in glass tubes for BET measurement allows one to measure the morphological information of the TiO_2 networks more precisely. As shown in Table 1, the surface area of the film was increased and the pore volume decreased with decreasing nanoparticle size. The amount of the dye adsorbed on the TiO_2 surface seemed to follow the variation of the surface area. Pore size distributions of the three samples calculated using the BJH model from respective nitrogen sorption isotherms provided a clear indication of these variations. As shown in Figure 4, the increase in the peak pore size with larger nanoparticles would be a main reason for the variation of the surface area and pore volume. While the relation between surface area and pore radius (size) is a first order relationship, pore volume increases in proportion to the cube of a pore radius, suggesting that large pores become dominant in determining pore volume. As a result, the 20 nm nanoparticle film showed the highest pore volume as it had larger pores than the others.

Table 1. Surface Areas and Pore Volumes Determined by Multi-Point BET and BJH Models and Corresponding Dye Loading for the TiO_2 Nanoparticle Films, Respectively

	surface area (m^2g^{-1})	pore volume (ccg^{-1})	dye loading ($mgcm^{-2}$)
TiO_2 nanoparticle, 20 nm	83.8	0.478	0.139
TiO_2 nanoparticle, 15 nm	88.5	0.416	0.166
TiO_2 nanoparticle, 10 nm	102.4	0.371	0.182

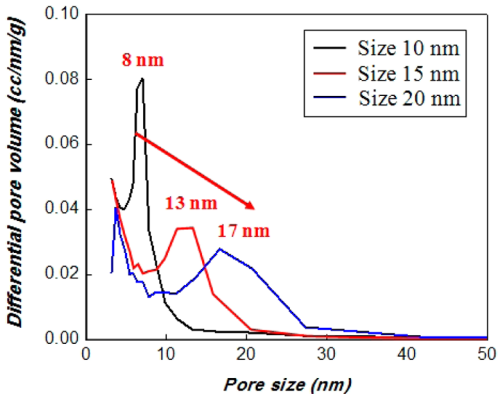

Figure 4. Pore size distribution of the different sized TiO_2 nanoparticle films determined by the BJH model. The peak pore size was revealed to be a little smaller than the nanoparticle size.

From the pore volume, the porosity of a film can be calculated using eq 1.[23]

$$P = V_p/(\rho^{-1} + V_p) \quad (1)$$

where V_p is a cumulative pore volume and ρ^{-1} is the reciprocal of the density of anatase TiO_2 (0.257 cm^3/g). The calculated porosities of the 20, 15, and 10 nm nanoparticle films were revealed to be 65, 62, and 59%, respectively. This range of porosity (50–65%) was known to have similar coordination number (N_n, ~ 4), suggesting that under multiple trapping condition (i.e., delayed electron diffusion), the coordination number of 4 would be sufficient to provide pathways without any constraints arising from a film morphology for electron transport.[24]

For the structural analysis on the TiO_2 networks, it can be concluded that only the particle size and surface area of the TiO_2 network would be the main factors affecting charge transport properties among the ones discussed above when the TiO_2 particle size was varied. The contributions of these morphological factors to charge transport properties were discussed in the next section.

Investigation of Charge Transport Properties. Electrochemical impedance spectroscopy (EIS) has proved to be a powerful tool in characterizing charge transport properties of DSCs in other studies.[25−27] Specifically, all kinetic processes such as the transport resistance (R_t), recombination resistance (R_{ct}), and chemical capacitance (C_μ) occurring in DSCs could be investigated by EIS at the same time.[28,29] The Nyquist plot is a common form of EIS result, where three semicircles representing different charge transfer processes are commonly observed in DSCs: charge transfer at the counter electrode/electrolyte interface in the range of 10^4–10^3 Hz, charge transfer at the oxide/electrolyte interface around 10^1 Hz (R_{ct}), and ion diffusion in the electrolyte below 10° Hz. Additionally, charge transfer from a FTO to oxide network, which could be detected above 10^5 Hz, and charge transport in the oxide network with the frequency range of 10^3–10^2 Hz (transport resistance, R_t) are not commonly observed as they are merged into R_{ct} due to the characteristic of $R_{ct} \gg R_t$.[30,31] Under conditions of low electron concentration in conduction band of an oxide (achieved through reduced bias voltage from the open circuit condition), R_t becomes larger and can be distinguished from R_{ct}, as shown in Figure 5a. With decreasing bias voltage, not only R_t and R_{ct} were increased but also R_t appeared clearly as a straight line, which enables R_t to separate from R_{ct} having the curvature characteristic. The transport resistance (R_t) was decreased with the particle size, indicating that the electron transport along the TiO_2 network got facilitated for the larger particle size. Figure 5a is the Nyquist plot measured at various bias voltage, showing an appearance and increase of R_t (the straight line in about 10^2 Hz region) from R_{ct} (the semicircle in low frequency region) of three photoanodes made of different sized nanoparticles. The transport resistance (R_t) denoting how effectively electrons move through the oxide network was at a maximum when the TiO_2 nanoparticle size was 10 nm and decreased with increasing the nanoparticle size, though no further decrease was observed for the size increase from 15 to 20 nm. The larger R_t of the 10 nm TiO_2 nanoparticle photoanode could be explained in terms of mean free path. As the coordination number is the same (~4) for three electrodes, electron transport along with a TiO_2 network can be simply discussed in one dimension, as shown in Figure 5c. Assuming that electrons move from left to right to be collected, the electrons have to pass through different numbers of boundaries for the same traveling distance depending on the particle size. As some of the electrons are reflected when the electrons meet boundaries, electrons in a small particle network are likely to have a shorter mean free path than electrons in a large particle network due to short travel distance before meeting boundaries and the high frequency of the number of electrons meeting boundaries to be collected at a FTO substrate. The almost same R_t for the 15 and 20 nm TiO_2 nanoparticles indicated that there is a saturation point for R_t in some range of particle size.[29]

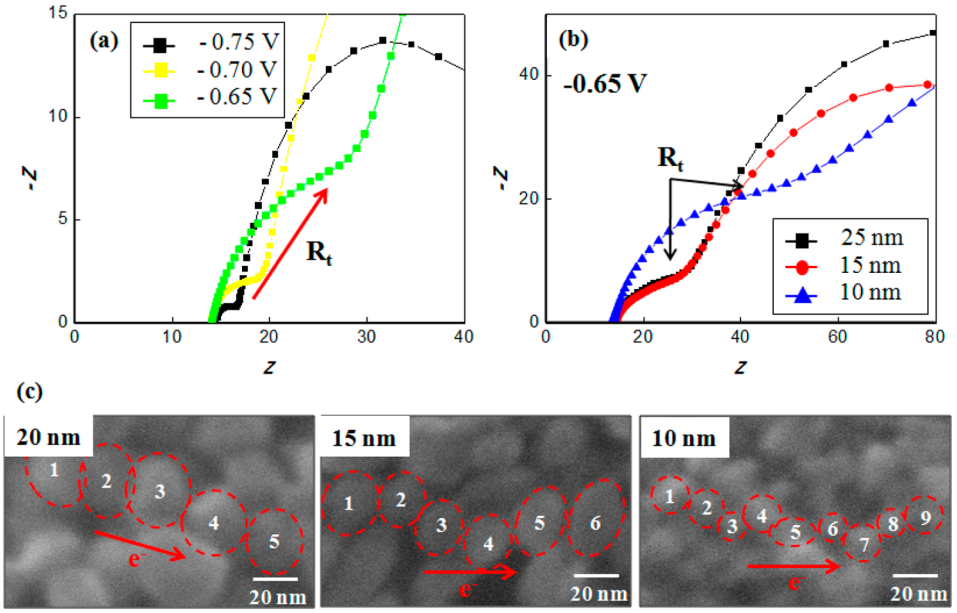

Figure 5. (a) Nyquist plot showing variation of transport resistance (R_t) with bias voltage and (b) transport resistances of the different sized TiO_2 photoanodes measured at −0.65 V; (c) SEM images showing the number of particles the electron passes through for a given distance.

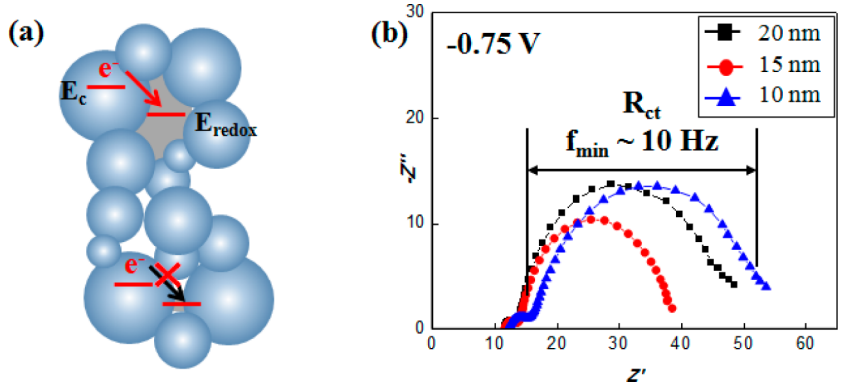

Figure 6. (a) Schematic illustrating effect of pore size on charge transfer resistance (recombination). The small pores might not contribute to electron transfer properly in terms of poor electrolyte penetration and/or ion transport and (b) charge transfer resistance (R_{ct}) of the different sized TiO_2 nanoparticle photoanodes, measured at −0.75 V.

When EIS measurements were carried out in the dark, the electrons in the TiO_2 network transfer to the oxidized species of the electrolyte (I_3^-) through the surface of the TiO_2 network; the surface should be in contact with the electrolyte. If there is no electrolyte as an acceptor, the recombination cannot occur, as schematically illustrated in Figure 6a. Figure 6b shows the charge transfer resistance (R_{ct}) with the minimum frequency of about 10 Hz, which decreased initially and then increased with a decreasing particle size, which is somewhat different from the monotonic increase of surface area with decreasing nanoparticle size. It is obvious that the first reduction of R_{ct} when the nanoparticle size was decreased from 20 to 15 nm would be ascribed to the increased surface area. However, rebounding of R_{ct} when the nanoparticle size was 10 nm even though the 10 nm particle film had the largest surface area seemed to be connected with the pore size distribution in terms of electrolyte penetration and/or iodide ions' transport. Although the exact mechanism or explanation for such experimental results is not available, the limited accessibility of small pores may be a possible cause. As shown in Figure 2, many pores in the 10 nm TiO_2 nanoparticle film might be too small to allow effective penetration of electrolyte and/or transport of iodide ions, leaving limited accessible pores (surface area) available for the charge transfer from the TiO_2 network to electrolyte. Similar observation or results have been reported in literature as well. For example, N3 dye (~1 nm) could not cover the TiO_2 surface fully when the TiO_2 particle size was in the range of 9−50 nm, and especially, the coverage of N3 dye for the 9 nm TiO_2 particle size became less than the others (20, 30, 50 nm particle sizes), indicating that the small pores limited N3 dye penetration.[21] Also, the pore size ranging from 18 to 24 nm exerts a strong influence on mass transport of ions in the $[Co(bpy)_3]^{II/III}$. Regeneration of oxidized dyes became less efficient with a decreasing pore size as a result of poor mass transport of ions in the electrolyte.[32] When considered only over 7 nm pores, it was revealed that only 32% of the total pore volume (21% pore surface area) is available for the 10 nm film, while there is about 45% pore volume (~25% pore surface area) for the 20 and 15 nm films. Similarly, the increase of SnO_2 nanoparticle size from 4.5 to 18 nm resulted in the enhancement of power conversion efficiency

by 200% as a consequence of the improved electrolyte penetration (more available surface area).[33]

While the real part of a Nyquist plot relates to various cell resistances, the imaginary part of a Nyquist plot provides information on chemical capacitance (C_μ). Due to the shielding by ions in the electrolyte, accumulation of charges (capacitance) in an oxide network of DSCs occurs without an electric field, indicating that the energy storage in a photoanode of DSCs is chemical and not electrostatic. Thus, the measured capacitance is related to the density of localized states (DOS) in the oxide network.[34,35] Even though the electron transport occurs predominantly in the conduction band, a measured diffusion coefficient of the TiO_2 nanoparticle photoanode was observed to be several orders of magnitude lower than that determined for the single TiO_2 anatase crystal as a result of many trapping−detrapping events of the electrons, commonly explained by the multiple trapping (MT) model.[36−38] Characterizing the localized states trapping electrons is important in determining charge transport properties occurring in a photoande of DSCs and could be possible through electrochemical methods like EIS and cyclic voltammetry (CV). It is known that the localized states distribute exponentially as follows;[39]

$$g(E) = \frac{N_L}{k_B T_0} \exp\left[\frac{E - E_c}{k_B T_0}\right] \quad (2)$$

where N_L is the total localized trap density, T_0 is a parameter with temperature unit that determines depth of localized states, E_C is the conduction band energy, and E is the trap energy. Figure 7 shows the capacitances of the three samples measured at various bias voltages by EIS.

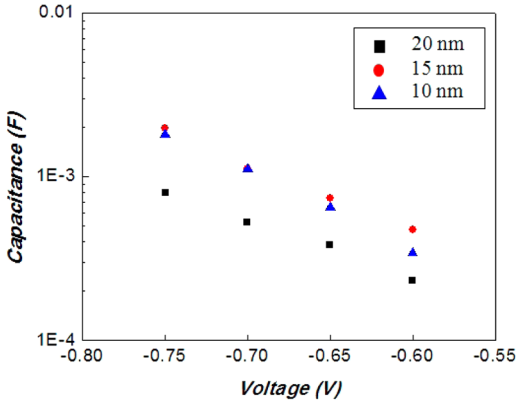

Figure 7. Chemical capacitance of the different sized TiO_2 nanoparticle photoanodes measured at various bias voltages by means of EIS.

As indicated in eq 2, the chemical capacitance denoting the number of electrons trapped at localized states showed exponential dependence on the applied bias voltage. The 10 and 15 nm nanoparticle films had nearly the same chemical capacitance, while the chemical capacitance of the 20 nm nanoparticle film was somewhat lower. The origin of the localized states is unknown, though it is commonly believed that the localized states are mainly located at and/or near the particle surface and around necks between particles. If correct, the structural parameters such as surface area and connection (neck) between particles exert a critical impact on not only charge transport properties but also the electronic structure of oxide networks.[29,40] Unlike our previous result for ZnO nanorod aggregates,[29] the chemical capacitance of the TiO_2 nanoparticle film seems to be more dependent on packing density of the TiO_2 nanoparticles and corresponding porosity and surface area of the network, instead of necks formed between the nanoparticles. In a given volume of the TiO_2 network, fewer TiO_2 nanoparticles would be packed as size of the TiO_2 nanoparticle is increased, making the TiO_2 network with low surface area. Thus, the 20 nm TiO_2 nanoparticle photoanode showed the lowest chemical capacitance as a result of the smallest number of the particles packed in the film and the corresponding lowest surface area,[18] whereas the similar chemical capacitance between the 15 and 10 nm TiO_2 nanoparticle photoanode seems to be the combined effect of surface area and necks formed between the TiO_2 nanoparticles. Due to the high thermal resistance of TiO_2,[41] it is hard to expect a remarkable difference in neck formation between the two nanoparticles; a minor contribution of the neck to the chemical capacitance would be compensated with the contribution coming from the small difference in the surface area, as shown in Table 1. To confirm the results on the chemical capacitance obtained by EIS, cyclic voltammetry (CV) tests were carried out and the results are shown in Figure 8. The exponential behavior of the cathodic current shown in Figure 8a denotes that the observed chemical capacitance follows eq 2 and the resultant chemical capacitance shown in Figure 8b displayed almost the same trends with the chemical capacitance measured by EIS, the lowest chemical capacitance for the 20 nm nanoparticle photoanode, and the same chemical capacitance for the 10 and 15 nm nanoparticle photoanodes.

The measured R_t, R_{ct}, and C_μ by EIS could be used to analyze charge transport properties in terms of electron lifetime (τ_n), diffusion coefficient (D_n), and diffusion length (L_n) as follows:[28]

$$\tau_n = R_{ct} C_\mu, \quad D_n = \frac{L^2}{R_t C_\mu}, \quad L_n = \sqrt{\tau_n D_n} \quad (3)$$

where L is a film thickness (7 μm, see Figure S2 in the Supporting Information). Figure 9a schematically explains charge transport phenomena occurring in the TiO_2 network. The electron movement in the conduction band contributing to electron transport (conductivity) suffers from the recombination and trapping−detrapping events which cause electron loss and delay in electron transport in conduction band, respectively. The equation $\tau_n = R_{ct} C_\mu$ in eq 3 indicates electron lifetime (recombination) involves two charge processes: electron movement to surface governed by a trapping−detrapping event (C_μ) and electron transfer at surface (R_{ct}). Therefore, electron lifetime (τ_n) was the longest for the 10 nm nanoparticle photoanode as a result of the highest R_{ct} and C_μ, while the 20 nm nanoparticle photoanode had the shortest electron lifetime even though the lowest R_{ct} was observed in the 15 nm nanoparticle photoanode because of the lowest C_μ. On the other hand, the highest diffusion coefficient (D_n) was achieved when the biggest nanoparticle (20 nm) was used, which was ascribed to the lowest R_t and C_μ. Like τ_n, the diffusion coefficient is also related to two charge processes: electron transport in the conduction band (R_t) and trapping−detrapping events (C_μ) delaying electron transport, as shown in eq 3. Thus, low R_t and C_μ results in high D_n. The effect of nanoparticle size on D_n supports the fact that the coordination number of the films with the porosity in the range of 50−65%

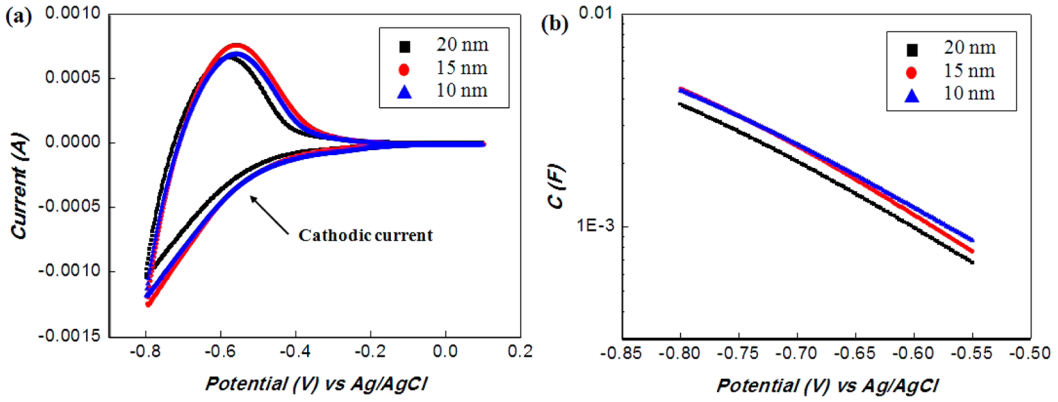

Figure 8. (a) Cyclic voltammograms of the different sized TiO_2 nanoparticle photoanodes and (b) the obtained chemical capacitance from panel a.

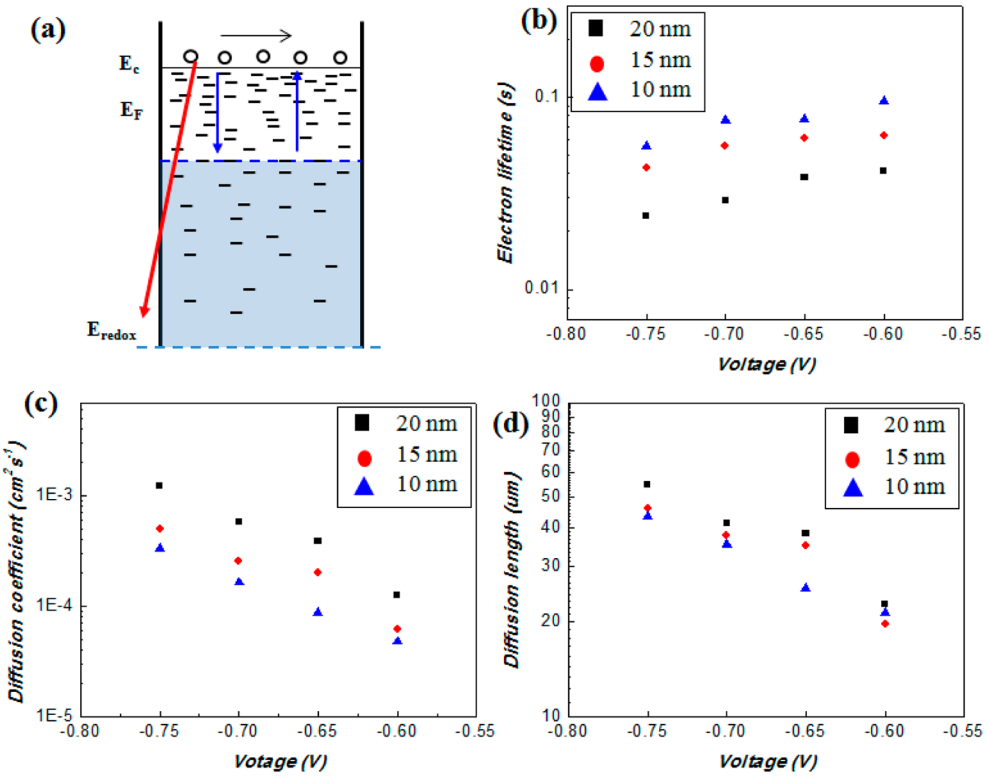

Figure 9. (a) Schematic showing kinetic processes of electrons in a TiO_2 nanoparticle network. (b) Electron lifetime (τ_n), (c) diffusion coefficient (D_n), and (d) diffusion length of the different sized TiO_2 nanoparticle photoanodes derived from the measured R_t, R_{ct}, and C_μ. In (a), black, blue, and red lines representing electron transport in conduction band, trapping−detrapping events, and recombination, respectively.

has the same contribution to electron transport because, if it works, porosity gives an inverse impact on D_n. Diffusion length (L_n), the average distance electrons in the conduction band diffuse before recombining, was shown in Figure 9d. From eq 3, it can be inferred that only R_{ct} and R_t give an impact on the determination of L_n because the C_μ related to trapping−detrapping events in τ_n and D_n cancel out. In other words, trapping−detrapping events delay not only D_n but also τ_n so the effects of C_μ on τ_n and D_n are compensated when determining L_n. The increase of L_n with increasing particle size implies that R_t exerts stronger impact on L_n than R_{ct}. As diffusion length (L_n) is directly related to charge collection efficiency (η_c), it is worthy to know how it affects DSC performances.

As the performances of DSCs show in Figure 10, the 10 nm photoanode had the poorest performance even though it had the highest surface area and dye loading as well as the highest resistance to recombination. It would be ascribed to the small pore size, not allowing the electrolyte penetration and/or ion transport in the electrolyte as well as the poor L_n. The observed increase in short circuit current density (J_{sc}) with increasing particle size seemed to be mainly related to the improved L_n, and the further increase in J_{sc} for the 15 nm photoanode compared to the 20 nm photoanode would come from the higher surface area, which resulted in good combination between light harvesting efficiency (LHE) and charge collection efficiency (η_c), leading to the highest efficiency, 5.6% (Table 2).[21,42,43] A similar relationship among particle size, dye loading, and efficiency was observed in the photoanode fabricated by electrophoretic deposition.[44] Therefore, in designing the structure of an oxide network for high performance of DSCs, attention to the roles of nanoparticle size, porosity, and pore size distribution on the competing

dx.doi.org/10.1021/am302781b | ACS Appl. Mater. Interfaces 2013, 5, 1044−1052

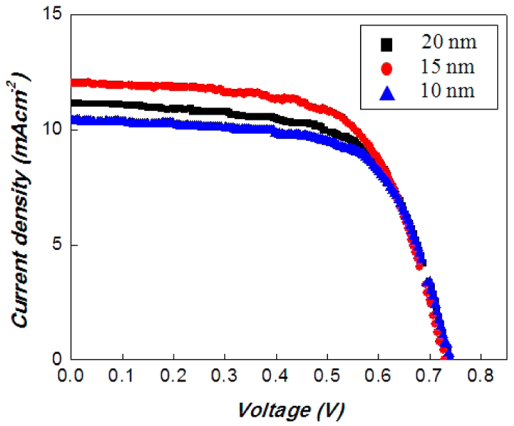

Figure 10. $J-V$ curves of three DSCs with photoanodes composed of 10, 15, and 20 nm TiO_2 nanoparticles, respectively.

Table 2. Performances of DSCs with Photoanodes Composed of the 10, 15, and 20 nm TiO_2 Nanoparticles Network

	V_{oc} (V)	J_{sc} (mAcm^{-2})	FF	η (%)
TiO_2 nanoparticle, 20 nm	0.74	11.1	0.64	5.2
TiO_2 nanoparticle, 15 nm	0.73	12.0	0.64	5.6
TiO_2 nanoparticle, 10 nm	0.74	10.4	0.65	5.0

considerations of surface area and charge transport is important; for a given saturated R_t and electrolyte-accessible pore size, higher surface area is favorable in terms of the effective surface area.

CONCLUSIONS

The structural variation of the TiO_2 nanoparticle photoanodes arising from the difference in nanoparticle size showed a substantial impact on the charge transport properties such as transport resistance (R_t) and recombination resistance (R_{ct}). The large particles were revealed to be favorable for charge transport by providing long diffusion path and less collision with boundaries. Also, the surface area should be considered in terms of the effective surface area (S_e) where the electrolyte is in contact, indicating that the pore size plays an important role in the performance of DSCs in terms of the penetration of the electrolyte. The highest power conversion efficiency achieved in the 15 nm nanoparticle photoanode suggests that maintaining the effective high surface area is important without consuming charge transport aspect (R_t).

ASSOCIATED CONTENT

Supporting Information

Optical image of glass tube containing TiO_2 network for BET measurement, SEM image showing the thickness of a TiO_2 film, and equivalent circuit used to fit the Nyquist plot. This material is available free of charge via the Internet at http://pubs.acs.org.

AUTHOR INFORMATION

Corresponding Author

*E-mail: gzcao@u.washington.edu.

Notes

The authors declare no competing financial interest.

ACKNOWLEDGMENTS

Most of the synthesis of nanostructures and electrical characterization was supported by the National Science Foundation (DMR-1035196) (K.S.P.), and some detailed structural characterization was supported in part by the US Department of Energy, Office of Basic Energy Sciences, Division of Materials and Engineering under Award No. DE-FG02-07ER46467 (Q.F.Z.).

REFERENCES

(1) O'Regan, B.; Grätzel, M. *Nature* **1991**, *353*, 737.
(2) Nazeeruddin, M. K.; Kay, A.; Rodicia, I.; Humphry-Baker, R.; Muller, E.; Liska, P.; Vlachopoulos, N.; Grätzel, M. *J. Am. Chem. Soc.* **1993**, *115*, 6382.
(3) Zhang, Q. F.; Chou, T. P.; Russo, B.; Jenekhe, S. A.; Cao, G. Z. *Angew. Chem., Int. Ed.* **2008**, *47*, 2402.
(4) Tiwana, P.; Docampo, P.; Johnston, M. B.; Snaith, H. J.; Herz, L. M. *ACS Nano* **2011**, *5*, 5158.
(5) Zhang, Q. F.; Cao, G. Z. *Nano Today* **2011**, *6*, 91.
(6) Meyer, G. J. *ACS Nano* **2010**, *4*, 4337.
(7) Hardin, B. E.; Snaith, H. J.; MaGehee, M. D. *Nat. Photo* **2012**, *6*, 162.
(8) Thavasi, V.; Renugopalakrishnan, V.; Jose, R.; Ramakrishna, S. *Mater. Sci. Eng. R* **2009**, *63*, 81.
(9) O'Regan, B. C.; Durrant, J. *Acc. Chem. Res.* **2009**, *42*, 1799.
(10) Boschloo, G.; Fitzmaurice, D. *J. Phys. Chem. B* **1999**, *103*, 2228.
(11) Wang, H.; He, J.; Boschloo, G.; Linddström, H.; Hagfeldt, A.; Lindquist, S.-E. *J. Phys. Chem. B* **2001**, *105*, 2529.
(12) Nakade, S.; Saito, Y.; Kubo, W.; Kitamura, T.; Wada, Y.; Yanagida, S. *J. Phys. Chem. B* **2003**, *107*, 8607.
(13) Du, L.; Furudo, A.; Yamamoto, K.; Hara, K.; Katoh, R.; Tachiya, M. *J. Phys. Chem. C* **2009**, *113*, 6554.
(14) Cass, M. J.; Qiu, F. L.; Walker, A. B.; Fisher, A. C.; Peter, L. M. *J. Phys. Chem. B* **2003**, *107*, 113.
(15) Gonzalez-Vazquez, J. P; Morales-Flórez, V.; Anta, J. A. *J. Phys. Chem. Lett.* **2012**, *3*, 386.
(16) Ansari-Rad, M.; Abdi, Y.; Arzi, E. *J. Phys. Chem. C* **2012**, *116*, 3212.
(17) Anta, J. A.; Morales-Flóres, V. *J. Phys. Chem. C* **2008**, *112*, 10287.
(18) Kopidakis, N.; Neale, N. R.; Zhu, K.; van de Lagemaat, J.; Frank, A. J. *Appl. Phys. Lett.* **2005**, *87*, 202106.
(19) Park, N. G.; van de Lagemaat, J.; Frank, A. J. *J. Phys. Chem. B* **2003**, *107*, 7759.
(20) Cass, M. J.; Walker, A. B.; Martinez, D.; Peter, L. M. *J. Phys. Chem. B* **2005**, *109*, 5100.
(21) Du, L.; Furube, A.; Hara, K.; Katoh, R.; Tachiya, M. *J. Phys. Chem. C* **2010**, *114*, 8135.
(22) Chou, T. P.; Zhang, Q. F.; Russo, B.; Fryxell, G. E.; Cao, G. Z. *J. Phys. Chem. C* **2007**, *111*, 6296.
(23) Benkstein, K. D.; Kopidakis, N.; van de Lagemaat, J.; Frank, A. J. *J. Phys. Chem. B* **2003**, *107*, 7759.
(24) van de Lagemaat, J.; Benkstein, K. D.; Frank, A. J. *J. Phys. Chem. B* **2001**, *105*, 12433.
(25) Bisquert, J. *J. Phys. Chem. B* **2002**, *106*, 325.
(26) Kern, R.; Sastrawan, R.; Ferber, J.; Stangl, R.; Luther, J. *Electrochim. Acta* **2002**, *47*, 4213.
(27) Bisquert, J.; Fabregat-Santiago, F.; Mora-seró, I.; Garcia-Belmonte, G.; Giménez, S. *J. Phys. Chem. C* **2009**, *113*, 17278.
(28) Wang, Q.; Ito, S.; Grätzel, M.; Fabregat-Santiago, F.; Mora-Seró, I.; Bisquert, J.; Bessoho, T.; Imai, H. *J. Phys. Chem. B* **2006**, *110*, 25210.
(29) Park, K.; Xi, J. T.; Zhang, Q. F.; Cao, G. Z. *J. Phys. Chem. C* **2011**, *15*, 20992.
(30) Hoshikawa, T.; Kikuchi, R.; Eguchi, K. *J. Electroanal. Chem.* **2006**, *588*, 59.
(31) Hoshikawa, T.; Yamada, M.; Kikuchi, R.; Eguchi, K. *J. Electrochem. Soc.* **2005**, *152*, E68.

(32) Kim, H.-S.; Ko, S.-B.; Jang, I.-H.; Park, N.-G. *Chem. Commun.* **2011**, *47*, 12637.
(33) Chappel, S.; Zaban, A. *Sol. Energy Mater. Sol. Cells* **2002**, *71*, 141.
(34) Bisquert, J.; Fabregat-Santiago, F.; Mora-seró, I.; Garcia-Belmonte, G.; Barea, E. M.; Palomares, E. *Inorg. Chim. Acta* **2008**, *361*, 684.
(35) Bisquert, J. *Phys. Chem. Chem. Phys.* **2003**, *5*, 5360.
(36) Forro, L.; Chauvet, O.; Emin, D.; Zuppiroli, L.; Berger, H.; Lévy, F. *J. Appl. Phys.* **1994**, *75*, 633.
(37) Tiedje, T.; Rose, A. *Solid State Comun.* **1981**, *37*, 49.
(38) Frank, A. J.; Kopidakis, N.; van de Lagemaat, J. *Coord. Chem. Rev.* **2004**, *248*, 1165.
(39) Jongh, P. E.; Vanmaekelbergh, D. *Phys. Rev. Lett.* **1996**, 3427.
(40) Hagfeldt, A.; Boschloo, G.; Sun, L.; Kloo, L.; Pettersson, H. *Chem. Rev.* **2010**, *110*, 6595.
(41) Park, K.; Zhang, Q. F.; Garcia, B. B.; Cao, G. Z. *J. Phys. Chem. C* **2011**, *115*, 4927.
(42) Schmidt-Mende, L.; Grätzel, M. *Thin Solid Films* **2006**, *500*, 296.
(43) Xi, J. T.; Al Dahoudi, N.; Zhang, Q. F.; Sun, Y. M.; Cao, G. Z. *Sci. Adv. Mater.* **2012**, *4*, 727.
(44) Xue, Z.; Zhang, W.; Yin, X.; Cheng, Y.; Wang, L.; Liu, B. *RSC Adv.* **2012**, *2*, 7074.